

Original Research Article

Microscopic imaging ellipsometry of submicron-scale bacterial cells

Mai Ibrahim Khaleel¹⁻³, Yu-Da Chen¹⁻³, Ching-Hang Chien¹⁻³ and Yia-Chung Chang^{1*}

¹Research Center for Applied Sciences, Academia Sinica, Taipei, 11529, ²Nano Science and Technology Program, Taiwan International Graduate Program, Academia Sinica and National Tsing Hua University, ³Department of Engineering and System Science, National Tsing Hua University, Hsinchu, 30013, Taiwan

*For correspondence: **Email:** yiachang@gate.sinica.edu.tw

Sent for review: 27 July 2017

Revised accepted: 23 October 2017

Abstract

Purpose: To demonstrate the power of microscopic imaging ellipsometry (MIE) to identify submicron-scale bacterial cells and track their surface topology variation.

Methods: Microscopic imaging ellipsometry with rotating compensator configuration was used to measure the ellipsometric spectra for dried submicron-scale *Streptococcus mutans* cells cultured on gold (Au) film for wavelengths (λ) in the visible range ($\lambda = 490 - 710$) nm. The ellipsometry characteristic images, Psi (Ψ), Delta (Δ), p- and s- polarized reflectance (I_p and I_s), and reflectance difference image (RDI) for a chain of two and four dried cells, were collected for a series of different objective planes (near the focal plane) for $\lambda = 600$ nm.

Results: The results show that by adjusting the position of objective planes (POP) to achieve the best focus, it was possible to identify cells smaller than $1 \mu\text{m}$ and observe their diffraction patterns in Ψ and Δ images. It was observed that Δ spectra and images were particularly sensitive to POP, while Ψ spectra and images for dried *S. mutans* cells were rather insensitive to POP.

Conclusion: MIE is a sensitive non-optical technique that can be used to image biological systems without the need for labeling of molecules.

Keywords: Objective plane, Imaging ellipsometry, Submicron-scale bacterial cells, *Streptococcus mutans*, Biosensing, Focal plane

Tropical Journal of Pharmaceutical Research is indexed by Science Citation Index (SciSearch), Scopus, International Pharmaceutical Abstract, Chemical Abstracts, Embase, Index Copernicus, EBSCO, African Index Medicus, JournalSeek, Journal Citation Reports/Science Edition, Directory of Open Access Journals (DOAJ), African Journal Online, Bioline International, Open-J-Gate and Pharmacy Abstracts

INTRODUCTION

Ellipsometry is an optical technique used to determine the thickness and optical constants of samples based on measuring two characteristic parameters, Ψ (Psi) and Δ (Delta), which describe the polarization contrast and phase change of light reflected from the sample [2]. The parameters Ψ and Δ represent the amplitude ratio and phase difference between p- and s-polarized light waves, which are related to the

complex Fresnel reflection coefficients according to Eq 1. [2-4].

$$\rho = \frac{r_p}{r_s} = \tan \psi e^{-i\Delta} \dots \dots \dots (1)$$

Throughout this paper, adopting the notations in physics community where the complex dielectric constant is defined as $\epsilon = \epsilon_1 + i\epsilon_2 = (n+ik)^2$ with n and k being the refractive index and extinction coefficient, respectively. We define the phase Δ

as given in Eq 1 instead of Δ as used in the optics community. With this notation, the sign convention of Δ in both optics and physics communities become consistent [5].

Microscopic Imaging Ellipsometry (MIE) combines the capabilities of ellipsometry in measuring thin film thickness accurately with the high spatial resolution of optical microscopy in lateral directions [6]. The technique is well known for being non-contact, non-destructive, and non-invasive [7-9]. It does not require special sample preparation nor labeling of molecules, in comparison to other detection techniques that require labeling- usually enzymatic or fluorescent such as fluorescence imaging [9-11]. Comparing MIE to other non-invasive and label-free imaging techniques like IR/thermal imaging [12], and Raman spectroscopy [13]. MIE provides submicron spatial resolution that cannot be achieved by IR/thermal imaging technique since it is based on detecting thermal radiation from the sample and not capable of extracting high-resolution structure information as MIE does [14]. Raman spectroscopy and MIE provide different but complementary information of the sample. MIE can detect very thin layers and measure their precise thickness, while Raman spectroscopy is sensitive to the chemical nature of the sample [13].

Streptococcus mutans (*S. mutans*) is an aerobic bacteria with a size ~ 800 nm and average height equals to 350 nm [14]. It has been known as the main etiological agent of dental caries and normal inhabitant of dental plaque [14]. In a previous work, we proposed microscopic imaging ellipsometry with rotating compensator configuration (MIE-RCE) as a sensing tool to detect the distribution of dried *S. mutans* cells on a glass substrate and determine their optical constants and thickness using theoretical models based on effective medium theory [14]. In this paper, we present MIE-RCE measurements of a chain of two and four dried *S. mutans* cells on Au film in specular reflection mode for wavelengths (λ) in the visible range ($\lambda = 490\text{nm} - 710\text{nm}$) on different objective planes. First, the MIE setup was calibrated for Au film, then the ellipsometry spectra of dried bacterial cells for different objective planes were measured at an angle of incident (AOI = 52°). A series of images for a chain of two and four dried *S. mutans* cells were captured for several objective planes, and images of Ψ , Δ , reflectance ($I_s = |r_s|^2$), p-polarized reflectance ($I_p = |r_p|^2$), and reflectance difference image ($RDI = I_s - I_p$) at 600nm were drawn by using the Intel Array Viewer Software [15]. Performing measurements

at different objective planes were done by moving the sample vertically via a motorized z-translation piezo stage (Physik Instrumente GmbH & Co. KG, Germany) [16].

The MIE images presented in this work of the two and four dried *S. mutans* cells are divided into intensity related images (I_p and I_s), polarization-contrast related images (Ψ and RDI), and phase related image (Δ) [17]. The intensity related images show the diffraction pattern outside the cells, the polarization-contrast related images give more information regarding the morphology of the cells, and the phase related image is sensitive to the refractive index and absorption coefficient of the cells. This study illustrates the versatility and the promise of MIE for future applications especially in the field of biological imaging since it enables us to identify submicron features, perform real-time measurements, and track the changes in biological systems without labeling the molecules.

EXPERIMENTAL

Cell culture and sample preparation

An *S. mutans* strain (ATCC 25175) and brain-heart infusion broth (BHI) were purchased from Creative Life Sciences (CMP), Taipei, Taiwan [18]. *S. mutans* was incubated in BHI medium shaken at 37 °C overnight. Another solution consists of 7.4 g BHI, 20 g sucrose, and 200 ml Millipore water was prepared to grow bacterial cells on Au film [19]. A substrate consists of SiO₂ 300 nm/ Ti 40 nm/ Au 50 nm was cleaned by sonication in acetone and isopropanol solutions for 30 and 20 minutes respectively. After that, the substrate was sonicated in Millipore water for 10 minutes and finally dried in the oven.

S. mutans was cultured on the Au film by immersing the cleaned substrate into a Petri dish contains 10ml of BHI-sucrose solution and 2.5 ml of incubated *S. mutans* cells in BHI medium. The Petri dish was sealed with parafilm and incubated for 6 h at 37 °C. After that, the substrate was washed three times with Millipore water and dried at room temperature for one day [14].

MIE-RCE setup

In this study, Optrel Multiskop system [20], was used to do the measurements. It based on the concept of rotating compensator ellipsometry. It consists of three main components: laser arm, sample stage, and detector arm as shown in Figure 1 [14]. The light source is generated from

a Fianium WhiteLase short wavelength supercontinuum laser with power >300 mW and wavelength from 400nm to 1000 nm [21]. The light beam then guided into a low-loss fiber connected to the laser arm of the system where a polarizer (Glan-Thompson Polarizing Prism, Germany) [22], is fixed at 45°. A rotating compensator is added to the laser arm and monitored by a goniometer. The compensator is a quarter-wave plate and rotates with the range of angles from 5° to 355° with 10° steps. The intensity of the incident light beam with spot size around 100 μm is enhanced by using a 10X lens before it hits the spot of interest on the sample.

(CCD) camera (Pixelfly qe) [24], with a pixel size equal to 164 nm.

The intensity of the reflected light beam from the sample collected by the CCD camera is then analyzed to determine the ellipsometric spectra and images. The sample stage of MIE-RCE consists of a motorized z-translation piezo stage fixed on a manual stage as shown in Figure 2. The motorized piezo stage is controlled by LabView program with 10 nm spatial resolution in the z-direction for fine adjustment. The manual stage has two fine adjustment controls for x- and y-directions with 10μm steps, and one coarse adjustment control for z-translation with 1mm spatial resolution [17]. The fine resolution in the z-direction is used for fine tuning of the objective plane $P1$ to $P4$ in Fig. 2 where $P1$ denotes the starting position of sample plane during the measurements, and by moving the sample stage up the objective planes reach $P2$, $P3$, and $P4$.

The scattered or reflected light from the sample is collected by an 80X objective lens with numerical aperture equals to 0.5, attached to the detector arm [23]. After that, the light beam passes through an analyzer mounted at 90° with respect to the polarizer [14]. Finally, the light beam is collected by a charge coupled device

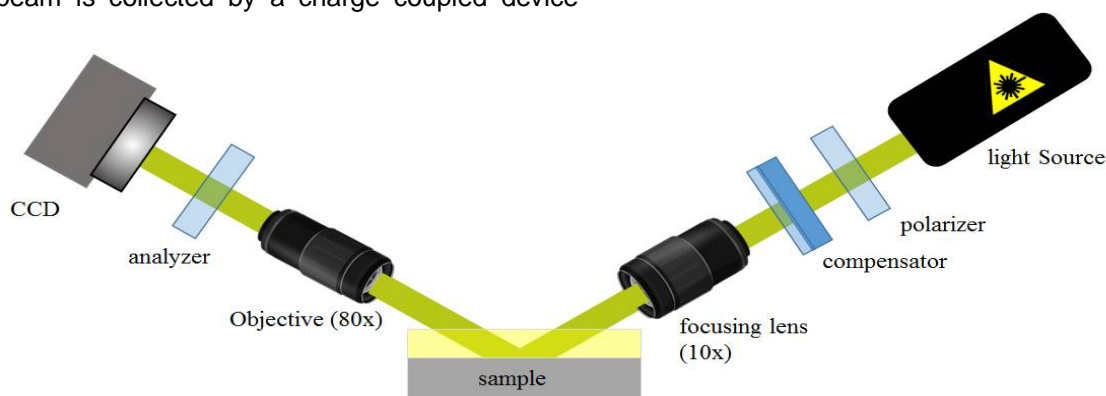


Figure 1: Schematic diagram of MIC RCE [14]

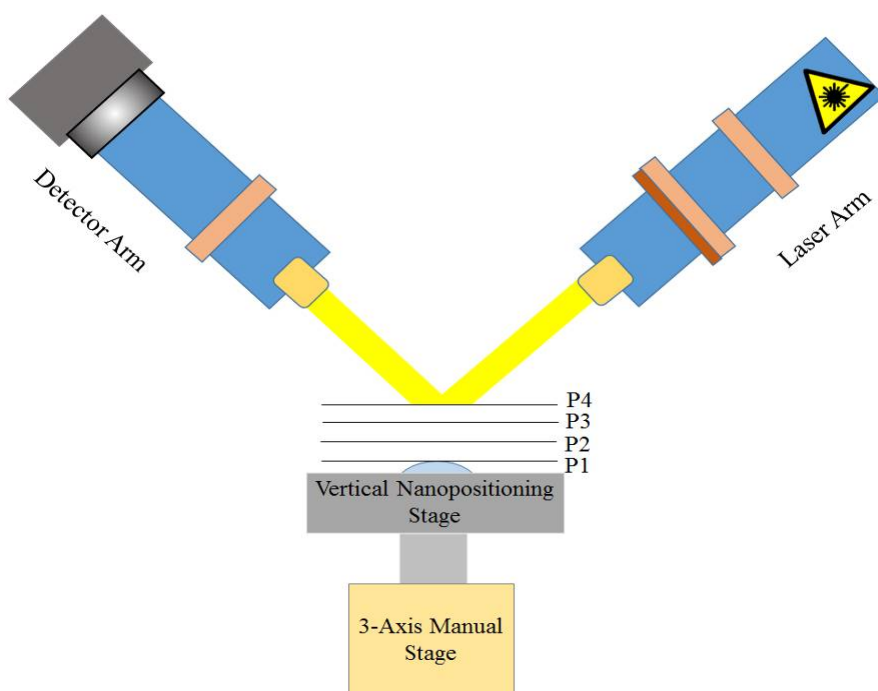


Figure 2: Schematic diagram of experimental setup using specular mode with different objective planes.

MIE-RCE calibration

To measure the ellipsometry spectra and images of any sample, MIE-RCE system must be calibrated first by using a flat substrate like glass, Si, or Au. For our calibration process, we used Si substrate, and another sample consists of glass/Ti 5 nm/Au 50 nm to calibrate the system. To make sure that we obtained the correct sign for Δ , we first measured the reflected light intensity of Si substrate and Au film as a function of compensator angle $I(\phi_c)$ in the visible range ($\lambda = 500\text{nm}$ to 700nm) integrated over an area equals to $20\mu\text{m} \times 20\mu\text{m}$. For Si substrate and Au film, we performed measurements for AOIs (72° , 82°) and (52° , 58°) respectively. The measured Ψ and Δ spectra for Si substrate and Au film by MIE-RCE were compared with Ψ and Δ spectra of the same Si substrate and Au film obtained by commercial V-VASE (J.A Woollam Co., United States) [25], for the same range of wavelengths and AOIs. For Si and Au film, we can use the single interface model to calculate the Fresnel reflection coefficients r_p and r_s for p - and s -polarized light [14], since Si and Au are opaque for the wavelength range considered here. We obtained

$$r_p = \frac{\frac{1}{c_0} \sqrt{\varepsilon_0 - \sin^2 \theta_0} - \frac{1}{c_1} \sqrt{\varepsilon_1 - \sin^2 \theta_0}}{\frac{1}{c_0} \sqrt{\varepsilon_0 - \sin^2 \theta_0} + \frac{1}{c_1} \sqrt{\varepsilon_1 - \sin^2 \theta_0}} \dots\dots\dots (2)$$

$$r_s = \frac{\sqrt{\varepsilon_0 - \sin^2 \theta_0} - \sqrt{\varepsilon_1 - \sin^2 \theta_0}}{\sqrt{\varepsilon_0 - \sin^2 \theta_0} + \sqrt{\varepsilon_1 - \sin^2 \theta_0}} \dots\dots\dots (3)$$

where θ_0 is the AOI, ε_0 and $\varepsilon_1 = (n + ik)^2$ are the dielectric constant of ambient (air) and Si or Au, respectively. Eqs. (2) and (3) was used to compute Ψ and Δ spectra for Si and Au film then compare with measured results obtained from V-VASE and MIE-RCE. In Figure 3a we show

values of optical constants n and k for Si substrate obtained by V-VASE fitting software, which fit Ψ and Δ spectra. While in Figure 3b we show values of optical constants n and k for Au film obtained by V-VASE fitting software, which fit Ψ and Δ spectra. Note that the fit takes into account the presence of 2nm thick SiO_2 on the Si surface, although its effect is negligible for the wavelength range (500nm-700nm) considered here. These values were used to calculate r_p and r_s (Eqs. (2) and (3)) for Si and Au film then obtain the theoretical values of Ψ and Δ without including the effect of oxide layer.

Figure 4 (a, b, c and d) show the comparison of Ψ and Δ spectra obtained by MIE-RCE, V-VASE, and theory for Si and Au film respectively. Figure 4 shows that both Ψ and Δ spectra of Si and Au film obtained by MIE-RCE, V-VASE, and theory (based on the single interface model) match well with each other in the full range of λ from 500nm to 700nm, indicating that the sign convention adopted in Eq 1 gives consistent results between our MIE-RCE setup and V-VASE.

RESULTS

Ellipsometry spectra and images were measured for two and four dried *S. mutans* cells cultured on Au film at different objective planes in specular reflection mode for $\lambda = (490 - 710 \text{ nm})$ at an AOI = 52° . The ellipsometry characteristic images Ψ , Δ , p - and s - polarized reflectance (I_p and I_s), and reflectance difference image (RDI) for the two and four dried cells were collected for a series of different objective planes and images at 600nm. To capture the images of the *S. mutans* cells, we used a CCD camera with pixel size equivalent to 82 nm under the 80X magnification mounted at detector arm of our Multiskop setup as shown in Figure 1 previously. To reduce the statistical error, we combine every 2×2 grids to form a pixel of $164 \times 164\text{nm}$, which gives more stable signal and better quality of MIE image. Both the

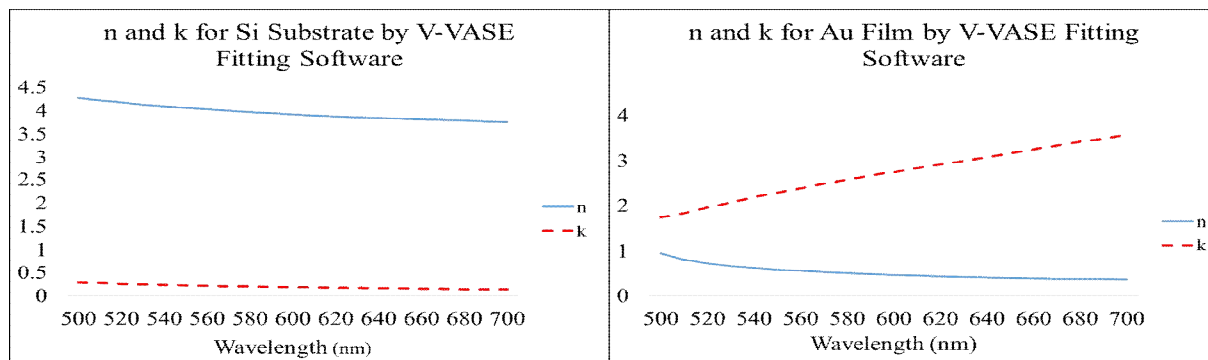


Figure 3: Optical constants n and k for (a) Si substrate, and (b) Au film obtained by V-VASE fitting software

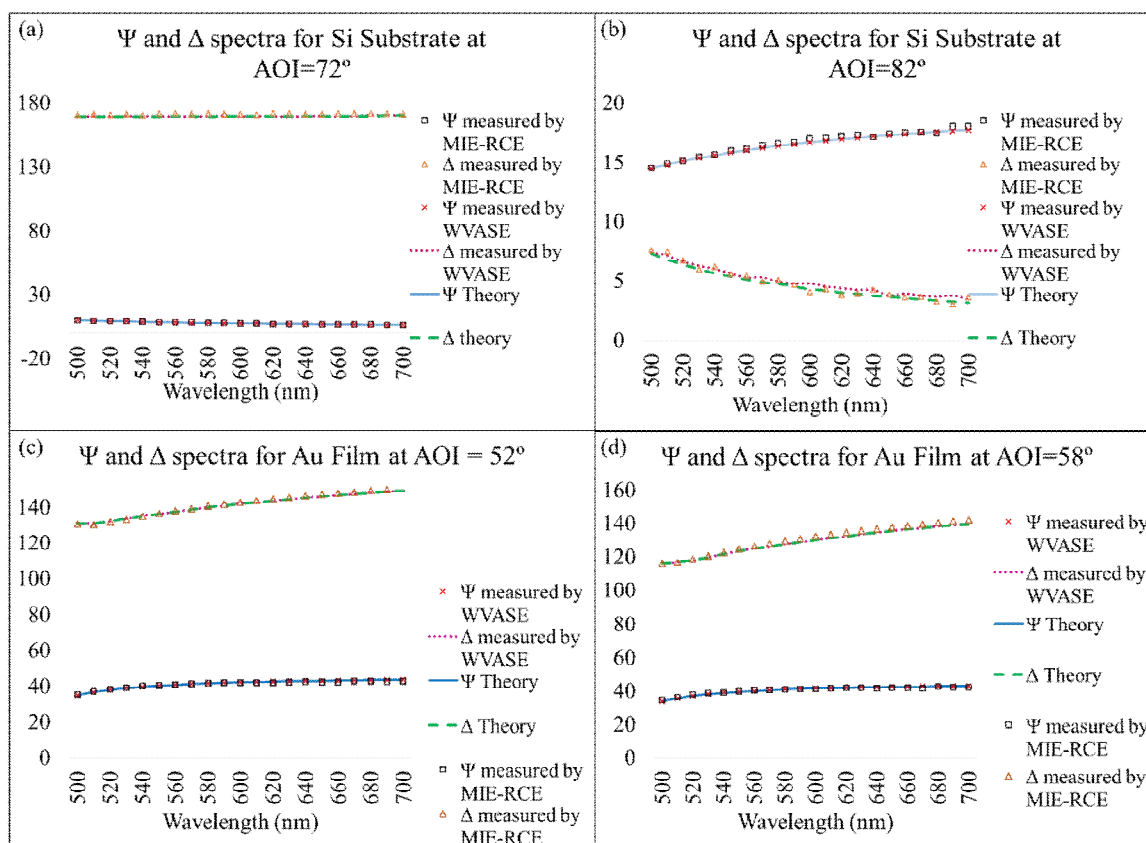


Figure 4: (a) Ψ and Δ for Si substrate obtained by MIE-RCE, V-VASE, and theory at AOI=72°, (b) Ψ and Δ for Si substrate obtained by MIE-RCE, V-VASE, and theory at AOI=82°, (c) Ψ and Δ for Au film obtained by MIE-RCE, V-VASE, and theory at AOI=52°, (d) Ψ and Δ for Au film obtained by MIE-RCE, V-VASE, and theory at AOI=58°

top view images of Δ in the x-y plane and the side view images of $-\Delta$ (from the detector arm) are shown to gain a better understanding. The units of the horizontal axis (y) in all the side view images of two and four dried *S. mutans* cells are pixels (one pixel = 164 nm).

MIE images for different objective planes of two *S. mutans* cells on Au film

The ellipsometry images Ψ , Δ , I_p , I_s , and RDI for two dried *S. mutans* cells on Au film collected at seventeen different objective planes are shown in Figure 5 ($P1 - P8$) and b ($P9 - P17$). The position of starting objective plane $P1$ is labeled 0, which is below the focal plane by several microns. We then moved up the sample with the motorized z-translation piezo stage. The advancement from the previous objective plane is labeled by +z, where z is the amount of movement in nm or μm . At objective planes $P1$ and $P2$ the two cells are still way out of focus, and the Δ image in Fig. 5 shows variation with magnitude of Δ varying within $\pm 40^\circ$ from a flat background (which is around 140°) as seen in the side-view of $-\Delta$ image.

After moving the sample up 200 nm ($P3$) Δ image begins to show a noticeable change in the middle of the two cells which appears as a small hole in the top view of Δ image. The side view of $-\Delta$ image shows a sharp peak at that position with the magnitude of $-\Delta$ deviate from the flat background more than 300° . This is caused by the interference effect of two diffraction fringes arising from the two cells, which becomes significant as the objective plane approaches the focal plane. The side-view $-\Delta$ images at $P4$, $P5$, and $P6$ show the increase in width of the sharp peak. At $P7$ and $P8$, the two cells became in focus (see CCD images), and Δ images show strong signals along the curved edge on the right side of the two cells, while I_p and I_s images of the same objective planes show two small spheres in the middle which are related to the two cells. It is noted that the width of the wall-like feature of the side-view $-\Delta$ image (along the y-axis) correlates directly with the length of the two cells when the objective plane coincides with the focal plane. It appears that the Δ image behaves like the gradient of the Ψ image, thus providing more sensitive detection of the boundary of the structure feature and it strongly depends on the position of the objective plane (POP).

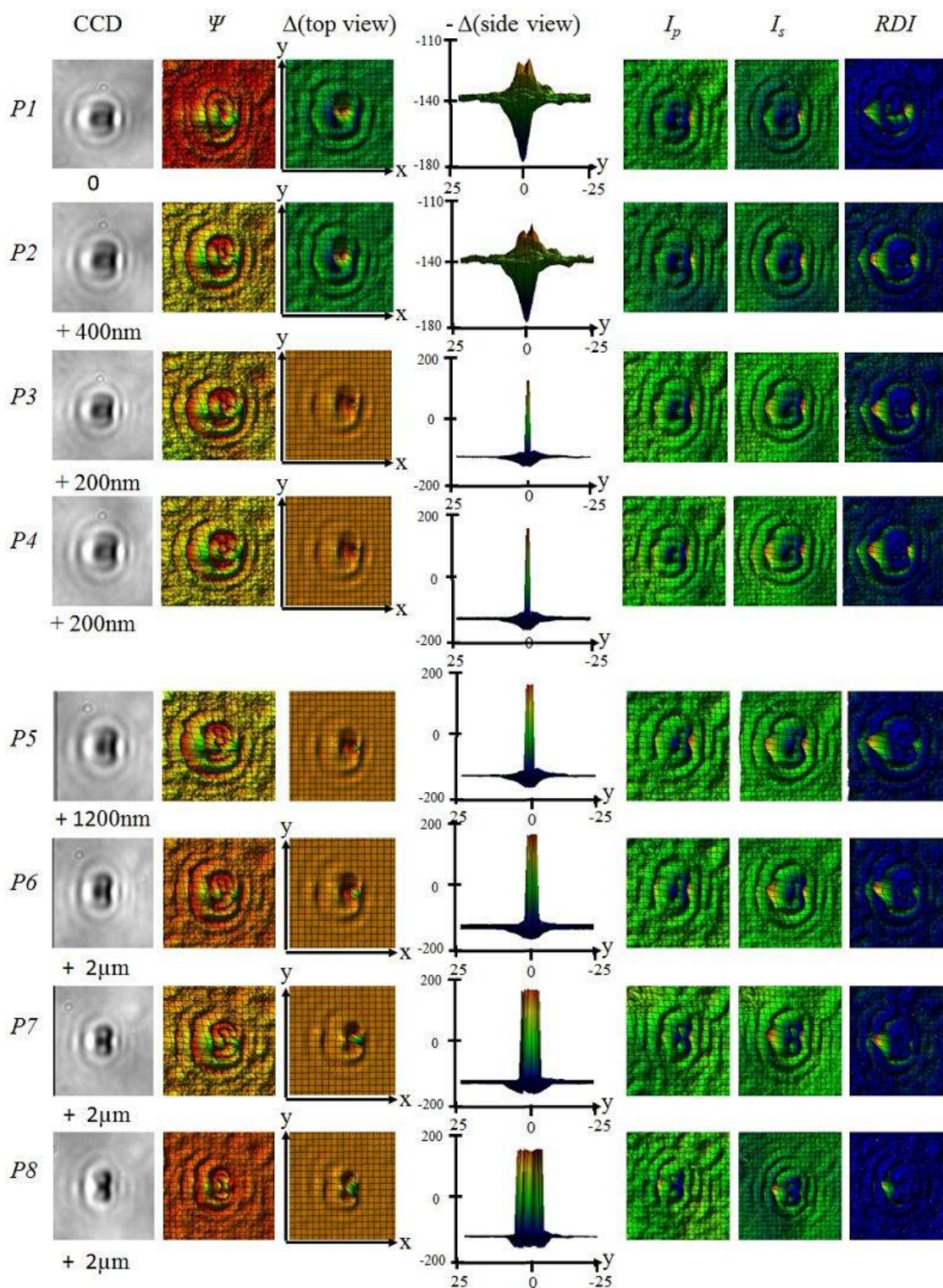


Figure 5: Ellipsometry images Ψ , Δ , I_p , I_s , and RDI of two *S. mutans* cells on Au film for different objective planes (P_1 – P_8) at AOI = 52°

In Figure 6, the objective planes P_9 , P_{10} , and P_{11} are above the focal plane, and the light penetrates through the two cells and gets reflected at the interface between the cells and the Au film. At P_{10} and P_{11} , the top-view Δ images show strong signals around the curved edges of the two cells and the side-view images

of $-\Delta$ show a widened wall-like structure which is related to the diffraction fringes of the two cells. Moving the stage further up from P_{11} leads to noticeable distortion in the curved edge (at P_{12} and P_{13}), and the Δ signal became weaker and weaker as the stage moves up. (See side-view $-\Delta$ images at P_{15} – P_{17}).

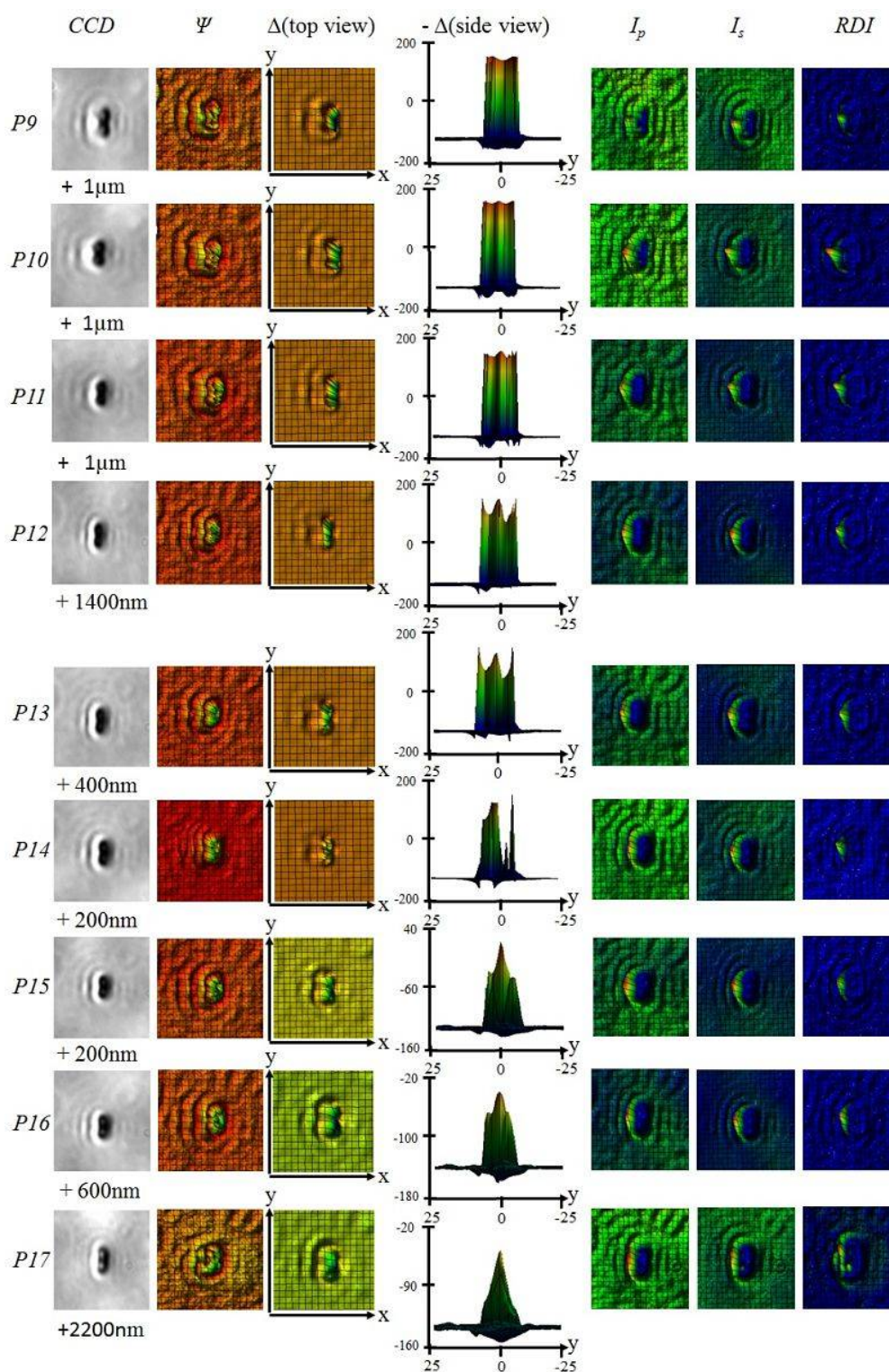


Figure 6: Ellipsometry images Ψ , Δ , I_p , I_s , and RDI of two *S. mutans* cells on Au film for different objective planes ($P9 - P17$) at $AOI = 52^\circ$

MIE images for different objective planes of four *S. mutans* cells on Au film

To illustrate that the sensitivity of Δ image to the POP for the two-cell case is not coincidental, we show the ellipsometry images Ψ , Δ , I_p , I_s , and RDI for a chain of four dried *S. mutans* cells on

Au film collected at nineteenth different objective planes are shown in Figs. 7 ($P1 - P8$), 8 ($P9 - P16$), and Figure 9 ($P17 - P19$). At $P1$, the four cells are way out of focus, and the Δ image shown in Figure 7 has weak variation (similar to $P1$ in Fig. 5). After moving the sample up 200 nm to $P2$, the Δ image exhibits significant change

near the first (lowest) cell of the four which appears as a sharp peak in the side view of $-\Delta$ image. Moving the stage up by 1800 nm to $P3$, we see a widened peak associated with the first cell in the side-view of $-\Delta$ image. Because the chain of four cells is curved with the lower end tilt toward the incident arm, only the Δ image of the first cell shows the significant change, since it is closest to the incident arm. At $P4$ a second hole

appeared at the last (highest) cell of the four in the top-view Δ image and the side-view of $-\Delta$ image shows a sharp peak, and the peak widened somewhat as the stage moved up slightly (by 600nm) to $P5$. At $P6$ a third hole (sharp peak) appeared in the top view of Δ image (side view of $-\Delta$ image), while at $P7$ and $P8$ the widths of all three peaks in the side view increased.

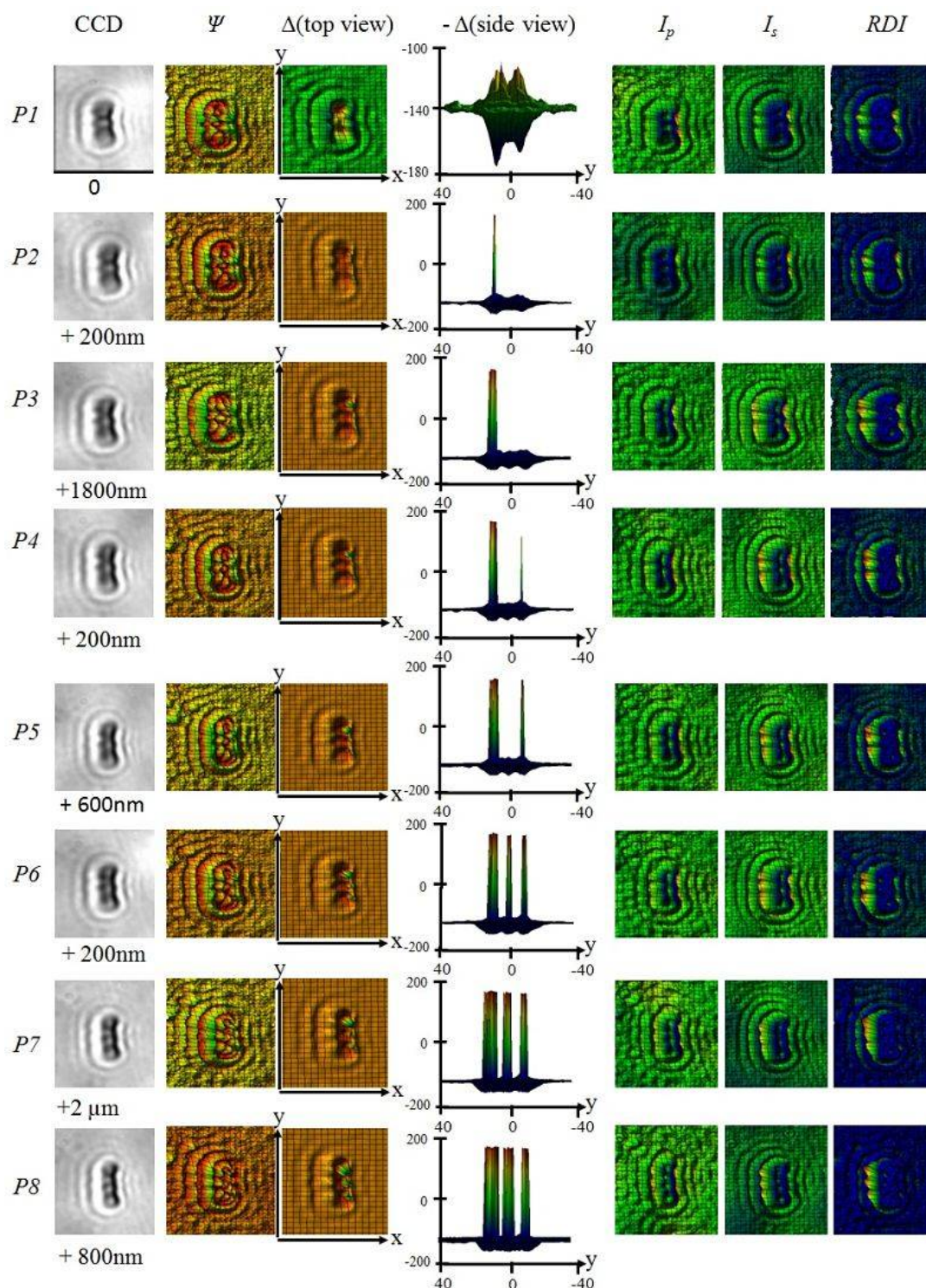


Figure 7: Ellipsometry images Ψ , Δ , I_p , I_s , and RDI of four *S. mutans* cells on Au film for different objective planes ($P1 - P8$) at $AOI=52^\circ$

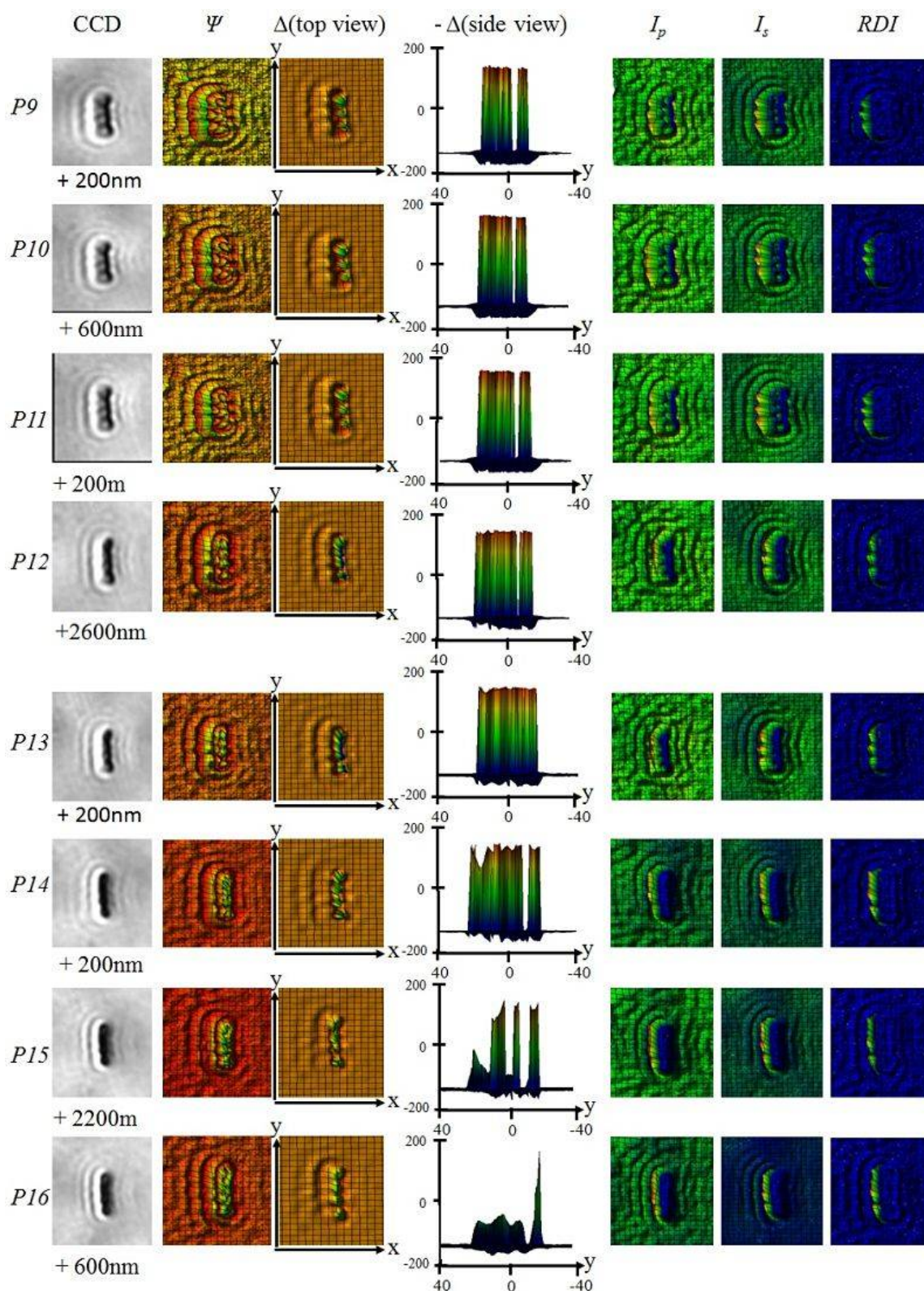


Figure 8: Ellipsometry images Ψ , Δ , I_p , I_s , and RDI of four *S. mutans* cells on Au film for different objective planes ($P_9 - P_{16}$) at $AOI=52^\circ$

We noticed that the width of the first peak (in the side view of $-\Delta$ image) is almost twice that of the second and third peaks, which is due to the newly picked-up signal from the second cell of the four. This conclusion is supported by the

CCD images and (the intensity related images I_p , I_s) at P_7 and P_8 that show a chain of four small spheres in the middle, which are related to four *S. mutans* cells.

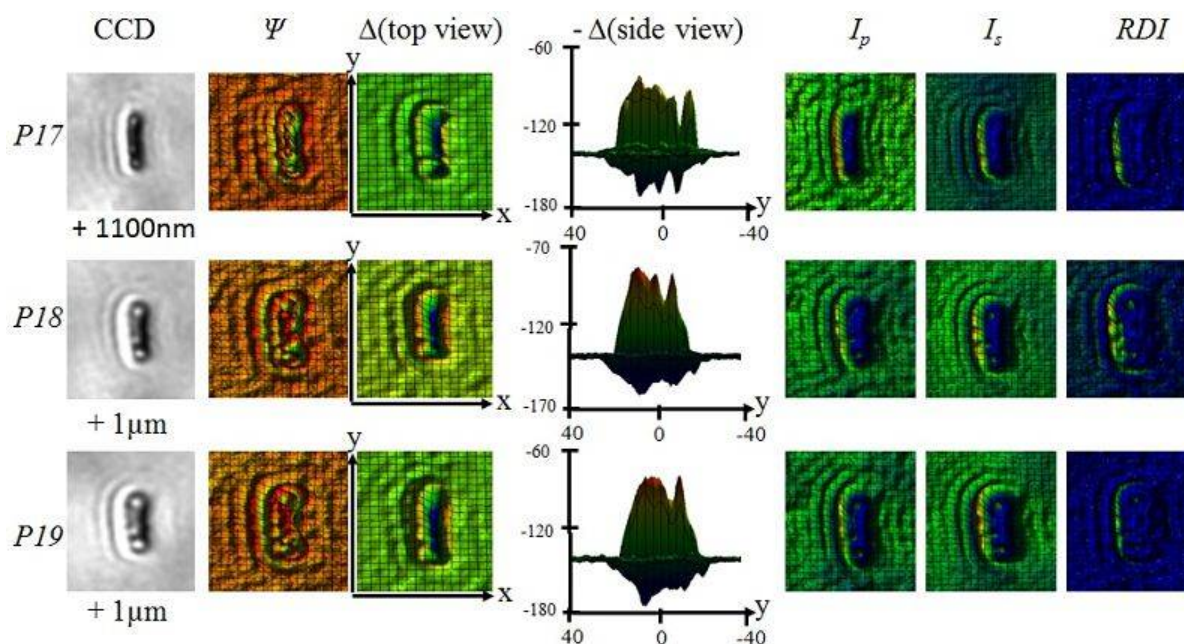


Figure 9: Ellipsometry images Ψ , Δ , I_p , I_s , and RDI of four *S. mutans* cells on Au film for different objective planes (P17– P19) at $AOI=52^\circ$

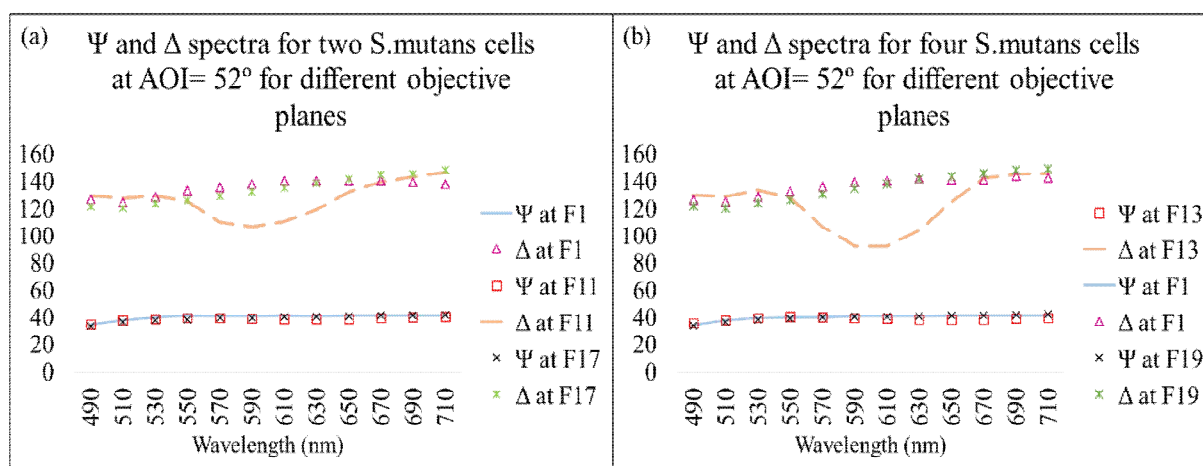


Figure 10: (a) Ψ and Δ for two *S. mutans* cells of Au film obtained by MIE-RCE at different objective planes P_1 (in Fig. 5), P_{11} , and P_{17} (in Fig. 6) at $AOI=52^\circ$, (b) Ψ and Δ for four *S. mutans* cells of Au film obtained by MIE-RCE at different objective planes P_1 , P_{13} , and P_{19} in Figure 7, Figure 8, Figure 9, respectively, at $AOI = 52^\circ$

At $P_9 - P_{11}$ the top-view Δ images show clear signals of curved edges of the four cells and the side-view of $-\Delta$ images show a nearly connected band (see Figure 8), which indicate these object planes are close to the focal plane and the depth of focus is around $1\mu\text{m}$. Meanwhile, the CCD image displays the shape of four cells. It is also noted that the width (along the y-axis) of the wall-like feature of side-view $-\Delta$ image correlates directly with the length of the four cells near P_{10} .

MIE spectra for different objective planes of two and four *S. mutans* cells on Au film

Finally, we show the ellipsometry Ψ and Δ spectra of two and four *S. mutans* cells on Au film for $\lambda = 490 \text{ nm} - 710 \text{ nm}$ at $AOI = 52^\circ$ in

At P_{12} and P_{13} , the focal plane is below the four cells, and light penetrated through the four cells and reflected at the interface between cells and the Au film, where the Δ images trace the outer profile of the four cells. Moving the stage further up to P_{14} and P_{15} , distortion occurred in Δ images which are related to the diffraction pattern of the curved edges of the four cells and the signal became weak as the stage move up (further away from the focal plane). Figures 10a and Figure 10b, respectively. For the two cells, the ellipsometry spectra integrated over an area equals to $3 \mu\text{m}$ (x-axis) \times $5 \mu\text{m}$ (y-axis) at three different objective planes P_1 , P_{11} , and P_{17} in Figure 5 and Figure 6, while for the four cells the ellipsometry spectra integrated over an area equals to $4 \mu\text{m}$ (x-axis) \times $9 \mu\text{m}$ (y-axis)

at three different objective planes $P1$, $P13$, and $P19$ in Figure 7, Figure 8 and Figure 9.

The Ψ spectra in Figure 10a and Figure 10b for two and four *S. mutans* cells at different objective planes are essentially the same, which indicates the Ψ images are not sensitive to the position of the objective plane. The Δ spectra for the two cells at $P1$ and $P11$ match each other in the range of $\lambda = 490$ nm to 710 nm, where the two cells are out of focus at these objective planes as shown in Figure 5 and Figure 6. For $P13$ (Figure 6) the two cells are slightly above the focal plane and benefited from the strong interference between the scattered wave and the reflected wave from the substrate, the measured Δ spectra of the two cells show different behavior in the range of $\lambda = 550$ nm to 650 nm, but remain similar to the ones at $P1$ and $P17$ in the range of $\lambda = (490 - 540$ nm) and (660 – 710 nm). Similar behavior for the Δ spectra of four *S. mutans* cells is seen in Figure 10b for the three different objective planes $P1$, $P13$, and $P19$. These results indicate that Δ spectra are also very sensitive to the position of the objective plane and the meaningful Δ spectra of *S. mutans* cells can be obtained only at the suitable objective plane.

From these results we noticed that Δ image results exhibit high sensitivity to the morphology of the object and the position of objective plane (POP), which allows the use of Δ images in the future to determine the accurate position of the focal plane and allow quantitative assessment of biological samples with submicron features. The

intensity related images (I_s , I_p) show complementary information to that obtained by Δ images. Δ images show a strong spatial variation in the side view (which delineates the structure feature) at objective planes close to the focal plane, while the polarization-contrast related images (Ψ and RDI) exhibit weak variation at these objective planes. The ellipsometry spectra results of two and four *S. mutans* also show the high sensitivity of Δ spectra to POP, while the Ψ spectra are nearly independent of the objective plane.

To get a close-up view of the Δ images, we show the 3D perspective of Δ images of two cells (at $P10$) and four cells (at $P13$) in Figure 11a and Figure 11b.

The 3D perspective of Δ images in Figure 11a and Figure 11b reveals the curved edges associated with the cells with two (four) curved edges appearing for the two (four) cells as indicated by red arrows. To give a better perspective, we have rotated the frame so that the detector arm is along the direction of the arrows. To lend further support to our analysis regarding the morphologies of the *S. mutans* cells, we show in Figure 8a an AFM topography image for a chain of four *S. mutans* cells on a glass substrate. We chose this image from a separate measurement where many AFM topography images were collected for *S. mutans* cells cultured for 24 hours on glass substrate.

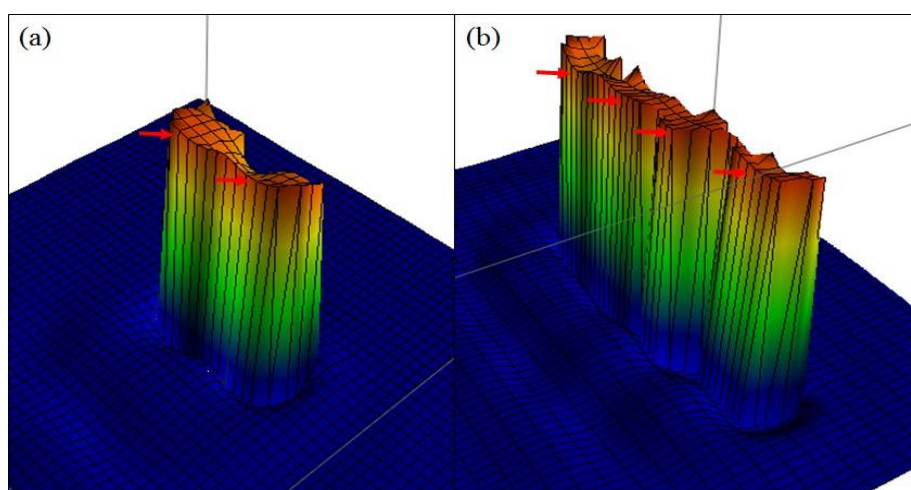


Figure11: 3D perspective of Δ images of (a) two *S. mutans* cells at $P10$, and (b) four *S. mutans* cells at $P13$

DISCUSSION

The findings show that the Δ images for two and four dried *S. mutans* cells exhibit big changes at different objective planes. Only at specific

objective planes (close to the focal plane) do the cells features appear clearly. These objective planes are just above the focal plane, and the interference of scattered light with the reflected light from the Au film is strongest.

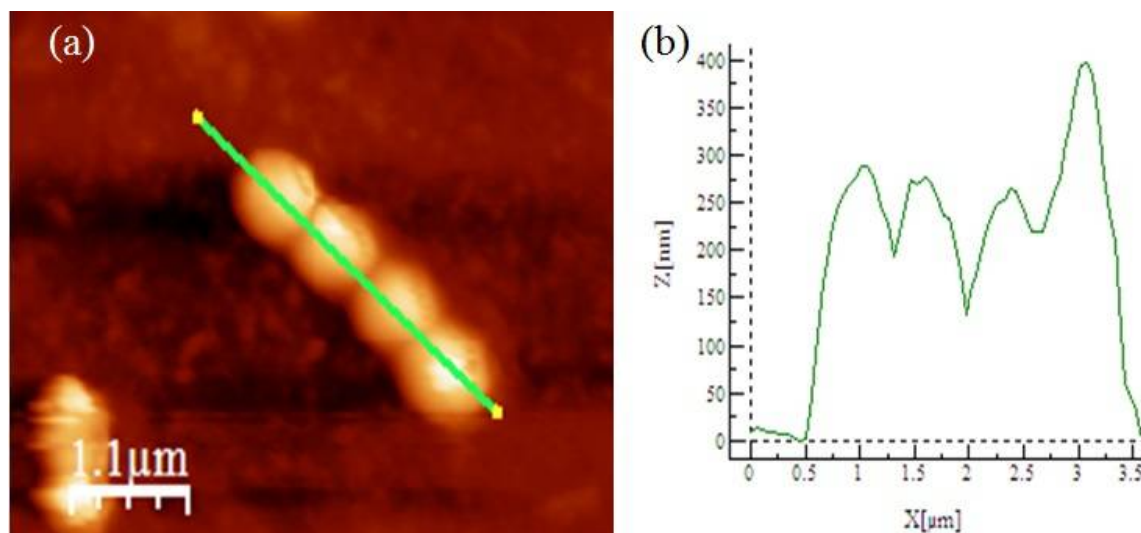


Figure 12: Four *S. mutans* cells on glass substrate after 24-h culture: (a) 5.7 μm x 5.7 μm AFM topography image, and (b) AFM profile height of the four cells

Figure 12b shows AFM height profile of the four *S. mutans* cells seen in Figure 11a. The height profile shows a size of 800 nm for each *S. mutans* cell, and the height of *S. mutans* cells ranges from 300 nm to 400 nm. Comparing with the AFM results of *S. mutans* cells, the prediction of cell dimension based on our ellipsometry Δ images is consistent, and it demonstrates that our MIE technique is capable of identifying submicron features (in this case *S. mutans* cell with 800 nm size).

CONCLUSION

The results obtained in this study show the power of MIE to identify sub-micron scale features, and track the diffraction patterns at different objective planes. This study reveals that MIE is a powerful sensitive imaging technique that can be used to study biological systems, since it is non-destructive, and does not require labeling of molecules like other imaging techniques. Furthermore, by incorporating theory simulation, based on the full solution to Maxwell equation for light scattering, it will be very easy to determine the shape of the sample beyond diffraction limit.

DECLARATIONS

Acknowledgement

This work was supported, in part, by the Ministry of Science and Technology of Taiwan under contract no. MOST 104-2112-M-001-009-MY2.

Conflict of Interest

No conflict of interest associated with this work.

Contribution of Authors

The authors declare that this work was done by the authors named in this article and all liabilities pertaining to claims relating to the content of this article will be borne by them.

Open Access

This is an Open Access article that uses a funding model which does not charge readers or their institutions for access and distributed under the terms of the Creative Commons Attribution License (<http://creativecommons.org/licenses/by/4.0>) and the Budapest Open Access Initiative (<http://www.budapestopenaccessinitiative.org/read>), which permit unrestricted use, distribution, and reproduction in any medium, provided the original work is properly credited.

REFERENCES

1. KG PIPGCP-ZPZS. [<https://www.physikinstrumente.com/en/products/linear-stages-and-actuators/piezo-stages/p-2611z-piezo-z-stage-201731/>].
2. Yoshizawa Tr. *Handbook of optical metrology: Principles and applications*. Boca Raton: CRC Press. 2009; xiii, p 730.
3. Bunshah RF. *Handbook of deposition technologies for films and coatings: science, technology, and applications*. 2nd edn. Materials science and process technology series Electronic materials and process technology. Park Ridge, N.J.: Noyes Publications. 1994. Xxvi, p 861.
4. Bubert H, and H Jenett. *Surface and thin film analysis: principles, instrumentation, applications*. Weinheim: Wiley-VCH. 2002. xvii, p 336.

5. Fujiwara H. *Principles of Spectroscopic Ellipsometry*, in *Spectroscopic Ellipsometry*. John Wiley & Sons Ltd, 2007; pp 81-146.
6. Ducheyne P. *Comprehensive biomaterials*. Amsterdam; Boston: Elsevier. 2011.
7. Dutta M, MS Rahman, AS Bhalla, and RY Guo. *Optical and microstructural characterization of multilayer Pb(Zr_{0.52}Ti_{0.48})O₃ thin films correlating ellipsometry and nanoscopy*. *J Mater Sci* 2016; 51(17): 7944-7955.
8. Peled A. *Photo-excited processes, diagnostics, and applications: fundamentals and advanced topics*. Boston: Kluwer Academic Publishers. 2003; xv, p 370.
9. Arwin H. *Spectroscopic ellipsometry and biology: recent developments and challenges*. *Thin Solid Films* 1998; 313: 764-774.
10. Qavi AJ, AL Washburn, JY Byeon, and RC Bailey. *Label-free technologies for quantitative multiparameter biological analysis*. *Anal Bioanal Chem* 2009; 394(1): 121-135.
11. Arwin H. *Ellipsometry on thin organic layers of biological interest: characterization and applications*. *Thin Solid Films* 2000; 377: 48-56.
12. Jones AC, and MB Raschke. *Thermal Infrared Near-Field Spectroscopy*. *Nano Letters* 2012; 12(3): 1475-1481.
13. Lewandowska R, M Gaillet, GLe Bourdon, C Eypert, S Morel, C Naudin, and M Stchakovsky. *What can Raman spectroscopy and spectroscopic ellipsometry bring for the characterisation of thin films and materials surface? Surface and Interface. Analysis* 2008; 40(3-4): 588-592.
14. Khaleel MI, Y-D Chen, C-H Chien, and Y-C Chang. *Sensing of Streptococcus mutans by microscopic imaging ellipsometry*. *J Biomedical Optic* 2017; 22(5): 056005-056005.
15. *Informer Technologies, I Intel (R) Array Visualizer*. [cited 2017 Jan 2010]. Available from: <http://intel-r-array-visualizer.software.informer.com/2012.2010/>.
16. KG, PIPGC P-611.Z Piezo Z Stage. [cited 2017 Mar 2020]. Available from: <https://www.physikinstrumente.com/en/products/linear-stages-and-actuators/piezo-stages/p-2611z-piezo-z-stage-201731/>.
17. Chen Y-D, HY Hsu, MI Khaleel, Y-C Chang, C-H Wu, and H-C Wu. *Study of biological reaction in cancer cell with spectroscopic imaging ellipsometry*. *Proc. SPIE* 9925. 2016.
18. *Creative Life Science. Product category*, [cited 2017 Feb 2015]. Available from: <http://www.cmp-micro.com/>.
19. Hu Y, J Zhang, and J Ulstrup, *Interfacial electrochemical electron transfer processes in bacterial biofilm environments on Au(111)*. *Langmuir*, 2010. 26(11): 9094-9103.
20. O Optrel. *Ellipsometry*; [cited 2017 Jan 2025]. Available from: http://www.optrel.de/products_multiskop_ellipsometry.html.
21. FIANIUM, *WhiteLase SC series: blue & UV enhanced supercontinuum fiber lasers*. [cited 2017 Jan 2017] Available from: http://www.fianium.com/pdf/WhiteLase_SC2400_UV_v2011.pdf.
22. Fan JY, HX Li, and FQ Wu. *A study on transmitted intensity of disturbance for air-spaced Glan-type polarizing prisms*. *Optics Communic* 2003. 223(1-3): 11-16.
23. Inc, *EO Mitutoyo Infinity Corrected Long Working Distance Objectives*. [cited 2017 Mar 2024]. Available from: <https://www.edmundoptics.com.tw/microscopy/infinity-correctedobjectives/Mitutoyo-Infinity-Corrected-Long-Working-Distance-Objectives/>.
24. PCO *pixelfly qe*. [cited 2017 Jan 2020]. Available from: <https://www.pco.de/sensitive-cameras/pixelfly-qe/>.
25. Woollam, JA. *Vase ellipsometry*. [cited 2017 2003 2005]. Available from: <https://www.jawoollam.com/products/vase-ellipsometer>.